

Cryogenic temperature toughening and strengthening due to gradient phase structure

Zhiwei Ma, Yang Ren, Runguang Li, Yan-Dong Wang, Lingling Zhou, Xiaolei Wu, Yujie Wei, Huajian Gao



PII: S0921-5093(17)31568-X
DOI: <http://dx.doi.org/10.1016/j.msea.2017.11.107>
Reference: MSA35822

To appear in: *Materials Science & Engineering A*

Received date: 9 September 2017
Revised date: 24 November 2017
Accepted date: 26 November 2017

Cite this article as: Zhiwei Ma, Yang Ren, Runguang Li, Yan-Dong Wang, Lingling Zhou, Xiaolei Wu, Yujie Wei and Huajian Gao, Cryogenic temperature toughening and strengthening due to gradient phase structure, *Materials Science & Engineering A*, <http://dx.doi.org/10.1016/j.msea.2017.11.107>

This is a PDF file of an unedited manuscript that has been accepted for publication. As a service to our customers we are providing this early version of the manuscript. The manuscript will undergo copyediting, typesetting, and review of the resulting galley proof before it is published in its final citable form. Please note that during the production process errors may be discovered which could affect the content, and all legal disclaimers that apply to the journal pertain.

Cryogenic temperature toughening and strengthening due to gradient phase structure

Zhiwei Ma^{1,5}, Yang Ren², Runguang Li³, Yan-Dong Wang³, Lingling Zhou^{1,5}, Xiaolei Wu^{1,5}, Yujie Wei^{1,5*}, Huajian Gao^{4*}

¹State Key Laboratory of Nonlinear Mechanics, Institute of Mechanics, Chinese Academy of Sciences, Beijing 100190, China

²Advanced Photon Source, Argonne National Laboratory, 9700 S. Cass Avenue, Argonne, IL 60439, USA

³State Key Laboratory for Advanced Metals and Materials, University of Science and Technology, Beijing 100083, China

⁴School of Engineering, Brown University, Providence, RI 02912, USA

⁵School of Engineering Sciences, University of Chinese Academy of Sciences, Beijing 100049, China

Correspondence and requests for materials should be addressed to (Y. Wei) yujie_wei@lnm.imech.ac.cn or (H. Gao) huajian_gao@brown.edu.

Abstract

Cold embrittlement is one of the primary concerns challenging the usage of steels in infrastructures like pipelines and ocean platforms. This challenge is also compounded by the limited selection of materials for application in a cold and corrosive environment. Inspired by recent progresses in developing gradient structured materials with extraordinary properties, here we report a class of stainless steels with gradient phase structures achieving a superb combination of strength (1753MPa) and tensile ductility (>25%) at the cryogenic temperature of 77K. A set of cylindrical steel samples acquire a graded mixture of hard martensitic and soft austenitic phases through pre-torsion, which results in an optimal stress partition in the material - the hard martensitic structures showing a positive density gradient from core to edge carry higher stress near the edge, while the soft austenitic phase showing a negative density gradient from core to edge serves to retain substantial

tensile ductility. The phase-transformation at low temperature in gradient structures and the resulted work-hardening could be adopted to enhance the ductility and strength of widely used engineering materials for their applications in harsh environment.

Keywords: Cryogenic; toughening; strengthening; gradient; synchrotron high-energy X-ray diffraction

Accepted manuscript

1. Introduction

With increasing activities for deep sea exploration and long-distance pipeline transportation, there is a prevailing need to enhance the reliability of materials in cold and corrosive environments¹⁻³. In addition to economic losses, failure of critical materials and structures for these applications may also lead to environmental disasters. So far, steels are the primary material of choice for pipelines and ocean platforms, although their performance at low temperatures is not ideal.⁴ As temperature drops, a ductile-to-brittle transition occurs around -73°C for most steels.⁵ So far, a vast amount of research has been dedicated to improving the mechanical properties of steels because of their ubiquity in infrastructures.⁶ In addition to the conventional alloying techniques, recent research for advanced steels has also included the following strategies and their combinations: (1) Strengthening by second-phase particles with tunable shape and volume fraction. By controlling the morphology and dispersion of brittle but hard FeAl intermetallic compound, Kim et al.⁷ realized high strength and intermediate tensile ductility in high-aluminum low-density steel; (2) Introducing gradient microstructures for better load and deformation partition.⁸⁻¹¹ The idea may be traced back to the design motif of teeth and bones.^{12,13} It has been revealed that even a thin gradient layer introduced by a surface mechanical attrition treatment¹⁴ could substantially enhance the strength of interstitial free (IF)-steel.¹⁵ Wei et al. also demonstrated that twin-induced plasticity (TWIP) steel with linearly graded twin density can enhance the tensile strength of the material without reduction in ductility.¹⁶ (3) More recent investigations showed that Fe-based high-entropy alloys (HEAs) with more than four-elements in dominantly face-centred cubic phase exhibit ultra-high fracture-resistance in cryogenic conditions.^{17,18} This behavior was attributed to extensive hardening as a result of decreased phase stability known for advanced steels. A wide distribution of stacking fault energy in HEAs and the atomic level heterogeneity foster deformation-induced martensitic transformation,¹⁹ leading to outstanding mechanical properties and improved cryogenic performance; such small-scale level heterogeneity has also been adopted in amorphous metals for better toughness.^{20,21}

2. Experimental techniques

2.1 Mechanical behavior of gradient structure at cryogenic temperature

Here, we report a simple strategy of utilizing gradient phase structures to keep traditional stainless steels strong and tough at cryogenic temperatures, achieving properties comparable to those of advanced steel-based alloys but at much lower cost. We choose a commercially available 304 stainless steel for the study. The steel consists of primarily a single austenite phase. It is a face-centered cubic (F.C.C.) crystalline structure with 18% Cr, 8% Ni and balanced Fe in weight percentage, as tabulated in Table 1.

Table 1 | Chemical compositions of AISI 304 stainless steel

composition	C	Si	Mn	P	S	Ni	Cr	Fe
wt (%)	0.08	1.00	2.00	0.045	0.03	8.0	18	70.845

Following a method introduced by Wei et al.,¹⁶ we applied different amount of twist at room temperature (RT, defined as 300K) and cryogenic temperature (CT, taking here as the liquid nitrogen temperature of 77K) to cylindrical bars of AISI 304 stainless steel²². Subsequent tensile tests were carried at either RT or CT for samples with different amount of pre-twist at the two temperatures.

2.2 Phase transformation in gradient structure

The observed stress-strain responses could be connected to microstructural changes induced by the RT and CT pre-twists. For this purpose, we conducted high-energy synchrotron X-ray diffraction²³ and SEM observations to examine the variations in volume fraction of different phases along the radial direction of the cylindrical samples, and the technical details are supplied in Fig. 1.

We conducted high-energy synchrotron X-ray diffraction at beam line 11-ID-C of the Advanced Photon Source, Argonne National Laboratory (Fig. 1a). The wavelength of the X-ray is 0.0117418 nm and the distance from sample to a 2-D detector is about 1.8 m. The dog-bone-shaped in-situ tension specimen with a gage length of 10 mm and a width of 6 mm, is cut along longitudinal symmetrical plane of pre-twisted cylindrical bars, and polished to a final thickness of 0.5 mm (Fig. 1b). The ex-situ

specimen is cut from the cross-section of cylindrical bars with a radius about 5mm and a height about 2 mm. We applied ceria powders to specimen surface for the calibrations of beam centre, detector tilt, sample-to-detector distance, and instrument broadening. A displacement step of 150 μm within a beam cross-section of 100×300 μm^2 (Fig. 1d) was used between the adjacent scanning points, with a total of about 30 scanning points each sample from surface to core.

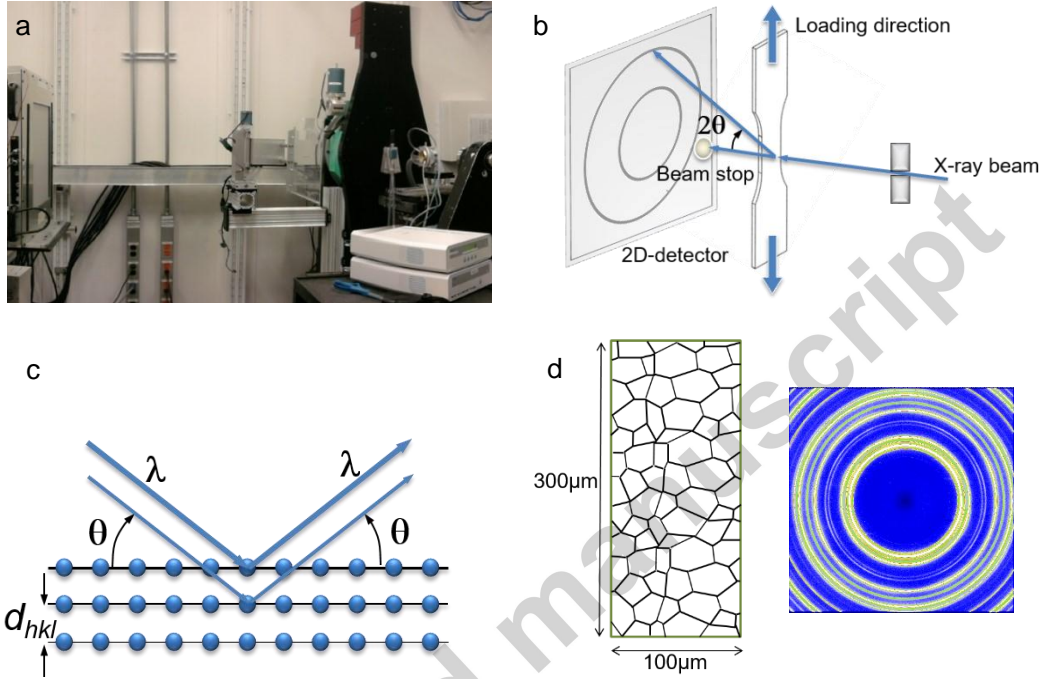


Figure 1 | Experimental setup for synchrotron high-energy X-ray diffractions. (a) The testing machine in the Advanced Photon Source, Argonne National Laboratory. (b) An illustration of the in-situ synchrotron high-energy X-ray diffraction experiment. (c) The theory of Bragg's law $\lambda = d_{hkl} \sin \theta_{hkl}$. (d) The transformation process of grain information to diffraction results.

The data were analyzed following the standard method by Young et al.²⁴ First we used a Fit2D program to translate the Debye diffraction rings into X–Y plots. The Bragg angle θ_{hkl} , peak width and integrated intensity of the $\{hkl\}$ plane were determined by fitting the individual single peak or overlapped peak in the diffraction spectra. d_{hkl} – the interplanar spacing of the $\{hkl\}$ plane, is obtained through Bragg's law, i.e. $\lambda = 2d_{hkl} \sin \theta_{hkl}$, where λ is the wavelength, θ_{hkl} is the diffraction angle of a Debye cone (Fig. 1c). The lattice strain is calculated from the d -spacing: $\varepsilon_{hkl} = (d_{hkl} - d_0)/d_0$ where d_{hkl} and d_0 are the d -spacings under a given load and

the reference state.

A MIRA3TM (LM) field emission scanning electron microscope from TESCAN was used for microstructure characterization. We used AZtec from Oxford Instruments at 20 kV to perform electron backscatter diffraction (EBSD) analysis for information on deformation twinning. Scanning the selected region of each image with a step size of 0.5 μm took approximately 20 minutes. At each location, an SEM image was captured in greyscale, and the corresponding EBSD image was captured in colour to reveal different crystallographic orientations.

2.3 Transmission Electron Microscope (TEM) observation

The dual beam focused ion beam/scanning electron microscopy (FIB/SEM) method was used to prepare the samples for transmission electron microscope (TEM) observation. The surface of the specimen was coated with platinum to prevent charging and to reduce damage from the ion beam. A dense beam of Ga⁺ ions was used to mill deep trenches in the specified regions. Then, foil was prepared in an orientation perpendicular to the radial direction by using the ion beam at an acceleration voltage of 30 kV and a maximum current of 20 pA to excavate on both sides of it. The foil (10 \times 5 \times 0.1 μm) was exhumed from the specimen's surface using an in-situ micro manipulator and transferred to a copper grid. Platinum soldering was used to attach the foil to the copper grid. After being mounted on the copper grid, the foil was ion-milled again to reduce its thickness to 50 nm. TEM observation was performed using a JEM-2100 transmission electron microscope operated at 200 kV. Images were recorded using a charge coupled device camera (2 k \times 2 k, Gatan 831) in binning mode two.

2.4 In-Situ synchrotron characterization

We further explored the phase-transformation and stress-distribution via in-situ synchrotron radiation experiments. For the interest of engineering applications and also limited by the capability of our facility, we considered samples pre-twisted at 233K. The pre-twisted samples were subjected to tension at either 233K or RT. We first applied RT tension to the 233K pre-twisted sample.

3. Results and Discussion

As shown in Fig. 2a, the RT yield strength of as-received 304 stainless steel is approximately 330 MPa. Before applying tension, we twisted the as-received cylindrical samples of 304 austenitic steel to different angles. The shear strain in the radial direction, γ , as a result of the pre-torsion, is $\gamma = \theta \times r/L$, where r is the radial position and θ is the net twist in a selected region with a uniform cross-sectional diameter and a length of $L = 60 \text{ mm}$. For a nominal pre-torsion of 180° , the maximum shear strain in a sample with radius $R = 5 \text{ mm}$ is approximately 0.26.

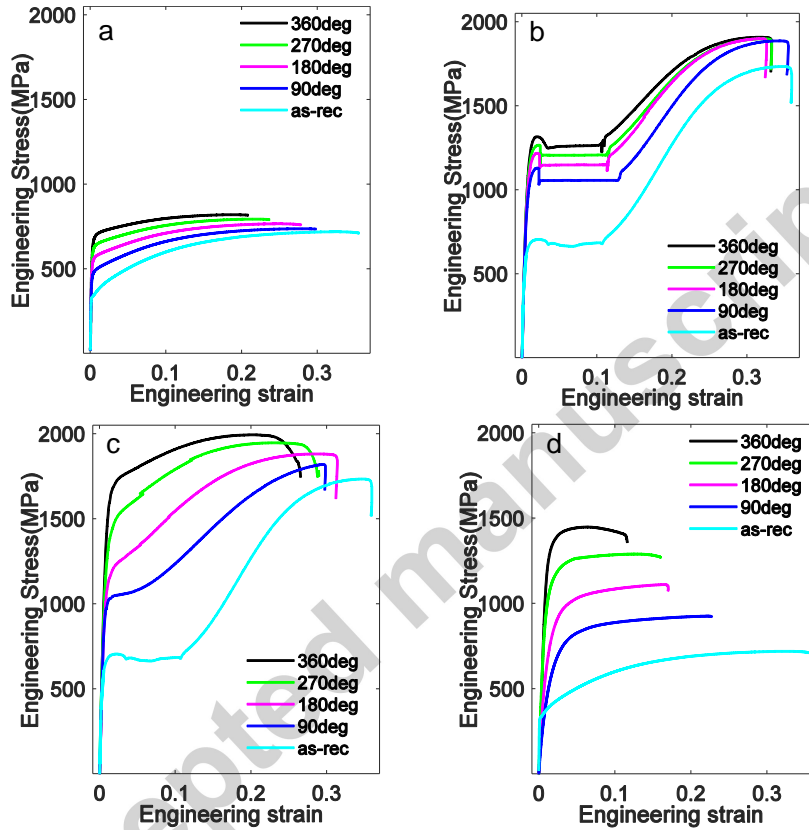


Figure 2 | Tensile stress-strain behavior of as-received and pre-twisted samples at different temperatures. (a) Tension at the temperature of 300K after torsion at the temperature of 300K. (b) Tension at 77K after torsion at 300K. (c) Tension at 77K after torsion at 77K. (d) Tension at 300K after torsion at 77K.

3.1 Stress-strain behavior

Figure 2 shows the tensile stress-strain behavior of the pre-twisted and as-received samples. A RT pre-twist increases the RT tensile strength: The RT yield strength of the as-received 304 stainless steel is 330 MPa, which is increased to 720 MPa by a 360° RT pre-twist, as seen in Fig. 2a. The increase in RT yield strength of the gradient samples was previously shown to enhance their RT fatigue

performance.²³ To further understand the influence of gradient structure on the mechanics behavior of the material at different temperature, we also test samples at 77K with pre-torsion at 300K. Their tensile stress-strain curves are shown in Fig. 2b. While the overall responses resemble those of the as-received one, pre-twisted samples at 300K have higher yield point and ultimate-strength, which have been increased from 671MPa and 1730MPa to 1264MPa and 1909MPa, respectively, by a 360° RT pre-twist. The strengthening is even more pronounced if the pre-twist was performed at CT, as seen in Fig. 2c. In this case, a 360° CT pre-twist increases the CT tensile yield strength to 1745MPa and the CT ultimate-strength to 1994MPa. If we change the processing sequence and apply torsion at CT first and then perform the tensile tests at 300K, the strengthening effects remains but ductility drops significantly, as demonstrated in Fig. 2d. The hardening exponent n of the CT tensile stress-strain curves after RT pre-torsion (Fig. 2b) and CT pre-torsion (Fig. 2c) are shown in Fig. 3a and Fig. 3b, respectively, where n is obtained from Hollomon's equation:²⁶

$$S = K\varepsilon^n \quad (1)$$

with S denoting the flow stress and K the strength coefficient. Even though n is usually considered to be a constant, it is strain dependent in this case. The high hardenability of samples at CT after torsion accounts for excellent ductility. Fig. 3c shows that this is in consistency with the previous research on 304 stainless steels.²⁷

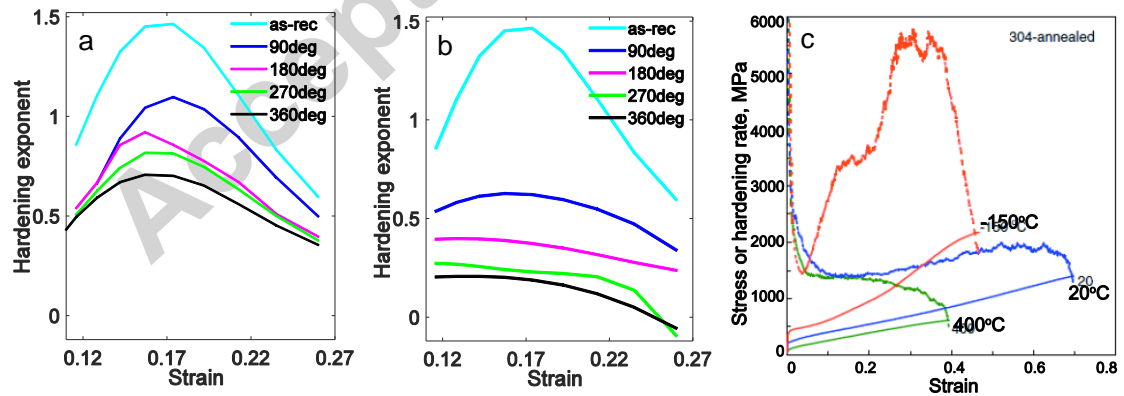


Figure 3 | The hardening exponent n of the tensile stress-strain curves (a) at 77K after torsion at 300K and (b) at 77K after torsion at 77K, where $S = K\varepsilon^n$, where S and ε are the flow stress and the plastic strain, and K is a material parameter. (c) Temperature dependence of the true stress–true strain curve (continuous line) and strain-hardening rate (dotted line) in annealed 304 stainless steel.²⁷

3.2 Phase evolution

Given that the average grain size is about $25\ \mu\text{m}$ and the typical spacing between X-ray diffraction spots is about $150\ \mu\text{m}$ within a beam cross-section of $100\times 300\ \mu\text{m}^2$, we could extract the distribution of the austenitic (face centred cubic, F.C.C.) phase and the martensitic phase from the X-ray diffractions. It is seen that a RT pre-twist gives rise to a mild negative gradient distribution in the austenitic phase, with smaller volume fraction near the surface; see Fig. 4a. The CT pre-twisted sample exhibits stronger gradients in both austenitic and martensitic phases, with positive gradient in B.C.C. phase but negative gradient in F.C.C. phase along the radial direction (Fig. 4b), indicating more severe phase transformation at CT than at RT.

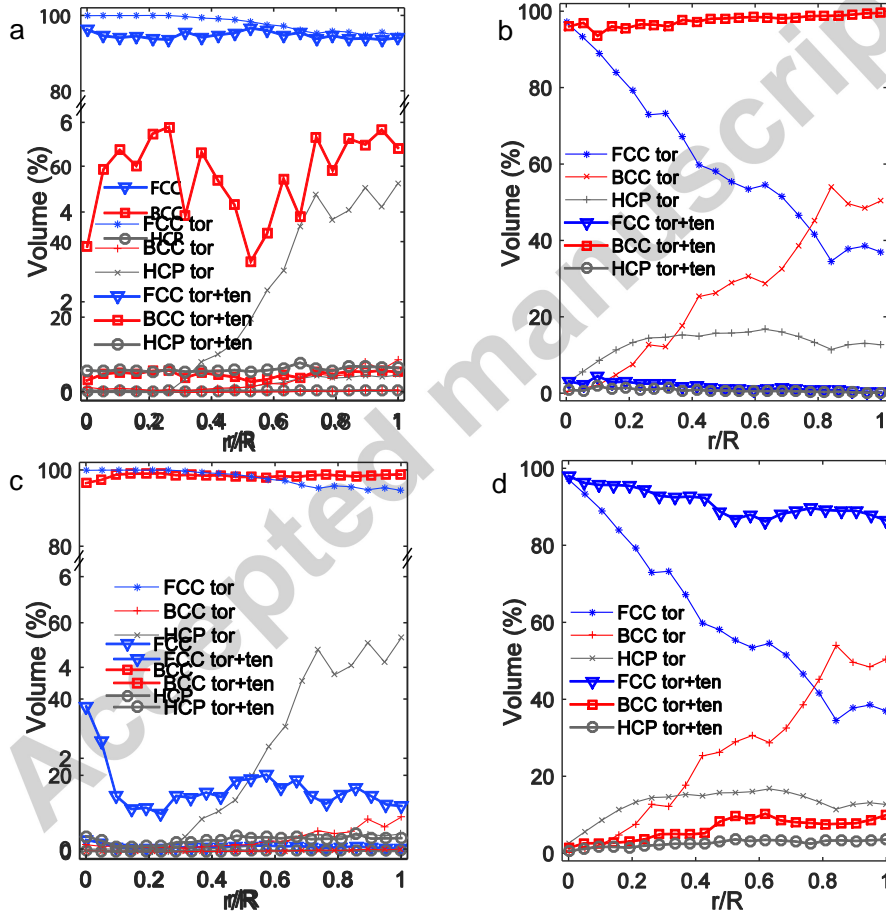


Figure 4 | Phase volume fraction evolution along the radial direction of the gradient sample. The samples were pre-twisted by 360 degree. (a) Tension at 300K to pre-twisted sample at 300K. (b) Tension at 77K to pre-twisted sample at 77K. (c) Tension at 77K to pre-twisted sample at 300K. (d) Tension at 300K to pre-twisted sample at 77K.

In contrast to the gradient distribution of F.C.C. and B.C.C. phases in the radial direction after a 360° RT pre-twist, subsequent RT tension smears out the gradient

(Fig. 4a). There is only a relatively small amount of phase transformation under RT tension. In comparison, there is a significant amount of austenitic to martensitic transformation under CT tension, as seen in Fig. 4c, and a gradient in phase distribution along the radial direction is clearly seen, suggesting that severe plastic deformation near the sample surface supplies nuclei for austenitic to martensitic transformation during subsequent tension. For CT pre-twisted samples, the RT tensile deformation gives rise to intermediate phase transformation accommodated plasticity; see Fig. 4d. Due to the presence of nearly 45% martensitic phase in the edge and a total of about 30% in the sample, the strength of the material is effectively enhanced, as seen in Fig. 2d, but its deformability is constrained by the incomplete phase transformation. In Fig. 4b, we show the radial distributions of phase volume in a 360° CT pre-twisted sample subject to CT tension, where most crystalline grains in the sample have been successfully transformed into martensites. In addition, the gradient becomes rather weak due to the thorough transformation. The initial high density stacking faults and gradient martensitic phase followed by subsequent full transformation lead to the observed high strength and high ductility behavior shown in Fig. 2c. Accompanied with the phase transformation, there is a high amount of H.C.P. phase, which is consistent with observations on phase transformation in austenitic stainless steel in other conditions.²⁸ In contrast, phase transformation in gradient samples is gradual (as proved by Fig. 5), which leads to mild yet continuous strain hardening during further deformation (Fig. 2c).

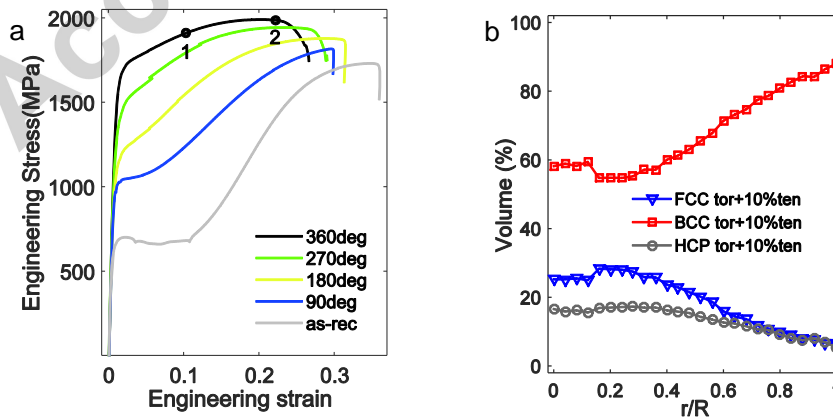


Figure 5 | Quantitative phase transformation during tensile testing at 77K after 360° pre-torsion at 77K. (a) Tensile stress-strain curves. (b) Synchrotron results measured at

10% tension (point 1 in a): in contrast to the volume fraction of different phases at point '2' (see Fig. 4b). Transformation in the gradient sample is gradual, leading to continuous hardening.

In addition to phase transformation accommodated plasticity, the austenitic phase in 304 stainless steel is also prone to twinning. We examined the twin deformation in the RT pre-twisted samples. Figs. 6a to c are EBSD pictures after a 360° CT pre-twist at three locations from $r=R$ to $r=0$, where the twin volume fractions are approximately 14%, 9% and 3%, respectively. Figs. 6d to f show EBSD images at different radial locations $r=R$, $r=R/2$ and $r=0$, where the twin volume fractions are approximately 9%, 4% and 1%, respectively.

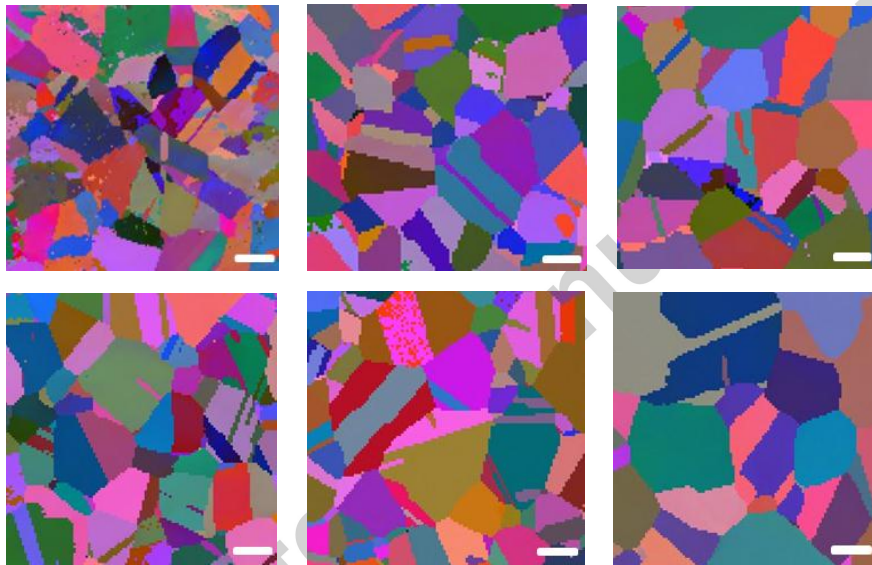


Figure 6 | Mechanical twist induced gradient structure in 304 stainless steel. (a) to (c) EBSD pictures at different locations of pre-torsion of 360° at 77K: $r=R$, $r=R/2$ and $r=0$, respectively. (d) to (f) EBSD pictures at different locations of pre-torsion of 360° at 300K: $r=R$, $r=R/2$ and $r=0$, respectively (scale bar: 10 μ m).

Figure 7 shows TEM pictures of pre-twisted samples after tensile failure. Fig. 7a demonstrates that when both pre-torsion and tension were conducted at RT, plastic deformation is primarily accommodated by deformation twinning. The thickness of laminar twins is rather small. In this case, the pre-twist induced gradient strengthens the material at reduced tensile ductility. In Fig. 7b, we see that the CT pre-twisted gradient sample has been almost completely transformed into martensites under CT tension, in consistency with our synchrotron radiation results in Fig. 4b. There are two types of grain structures in BCC phases, with randomly distributed grains (Fig. 7c)

and highly oriented laminar grains (Fig. 7d). Dense dislocations are seen in BCC grains, suggesting that in addition to the phase accommodated plasticity, dislocation mediated plasticity also plays an important role, as seen in Fig. 7e. In addition to the austenitic phase in the core stabilizing deformation as it is transformed into martensites, dislocations in hard and tough martensitic phases may also contribute to the superb combination of strength and ductility, as shown in Fig. 2c.

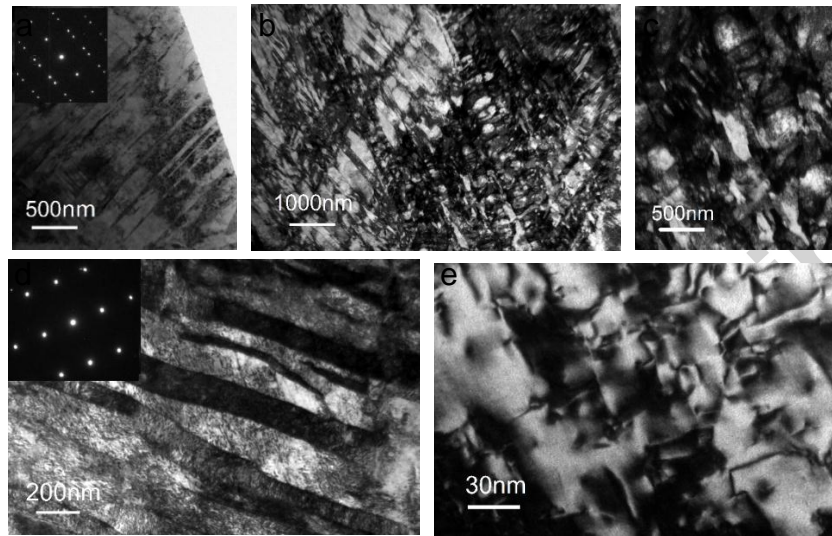


Figure 7 | TEM observation on the microstructures of pre-twisted samples after tensile failure. The samples were pre-twisted by 360 degree. (a) For the sample under tension at 300K and pre-twisted at 300K, deformation twinning is dominant. (b) to (e) Tension at 77K to pre-twisted sample at 77K. (b) Co-existence of laminar B.C.C. phases and ultrafine B.C.C. grains. (c) The amplified B.C.C. grains. (d) B.C.C. laminates with different orientations. (e) Dislocation patterns within a B.C.C. grain.

The phase mapping from EBSD pictures shown in Fig. 8 is also consistent with the TEM observation here. Here the samples were pre-twisted by 360 degree. The microstructure of a sample with tension at 300K after pre-twisting at 300K is shown in Fig. 8a. For comparison, that of the sample after tension at 77K (pre-twisted at 77K as well) is given in Fig. 8b. Their respective phase maps are presented in Fig. 8c and Fig. 8d, with twins in red, F.C.C. phase in blue, B.C.C. phase in green, and H.C.P. phase in yellow. While austenitic phase still is the dominant structure in the sample with tension and pre-twisting at 300K, the deformed sample after tension at 77K with pre-torsion at 77K is primarily composed of martensites, owing to the phase transformation

occurring at the pre-torsion and subsequent tension.

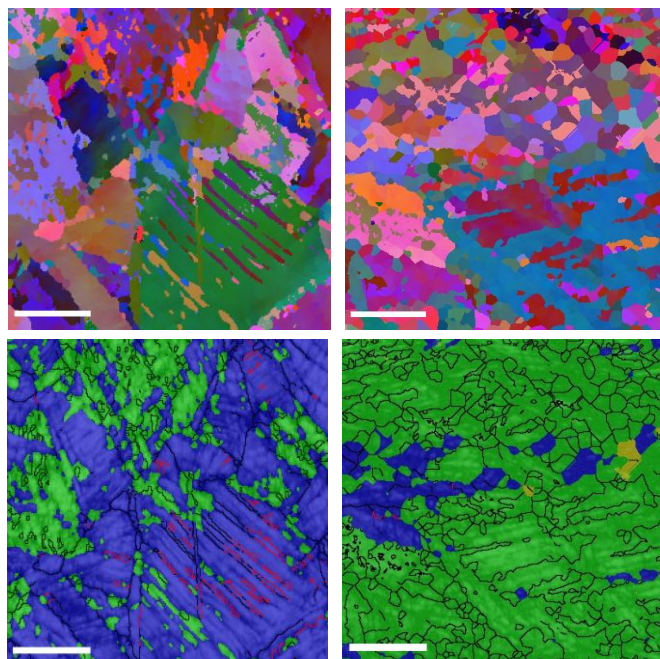


Figure 8 | Pre-twisted samples after tensile failure. The samples were pre-twisted by 360 degree. (a) Tension at 300K to pre-twisted sample at 300K. (b) Tension at 77K to pre-twisted sample at 77K. (c) to (d) Phase maps showing twin (red), F.C.C. phase (blue), B.C.C. phase (green), and H.C.P. phase (yellow) (scale bar: 5 μ m), with (c) corresponding to (a) and (d) corresponding to (b), respectively.

3.3 In-Situ synchrotron characterization

Along the radial direction, the intensity of the F.C.C. phase (Fig. 9a) decreases from core to edge at different strains, and the B.C.C. phase (Fig. 9b) varies in the opposite way. As an intermediate phase during F.C.C. to B.C.C. transformation, the intensity of an H.C.P. phase increases from a small value at the core to a maximum somewhere in the middle along the radial direction and then decreases to nearly zero at the edge, as seen in Fig. 9c. As the H.C.P. phase is intermediate during austenitic to martensitic transformation, the results in Fig. 9c may imply that the volume fraction of the H.C.P. phase is proportional to the transformation rate, in consistency with previous observations.²⁹ Figs. 9d to f show variations of the three phases when the 233K pre-twisted sample is subjected to tension at 233K. The trend of phase variation along the radial direction at different strains is similar to that seen in Figs. 9a to c, but their values are distinct. When tested under 233K tension, the intensity of the F.C.C.

phase is smaller than that at RT, as demonstrated by Figs. 9d and 9a. In contrast, the volume fraction of the H.C.P. phase is greater at 233K tension compared with that at RT, as seen in Figs. 9f and 9c.

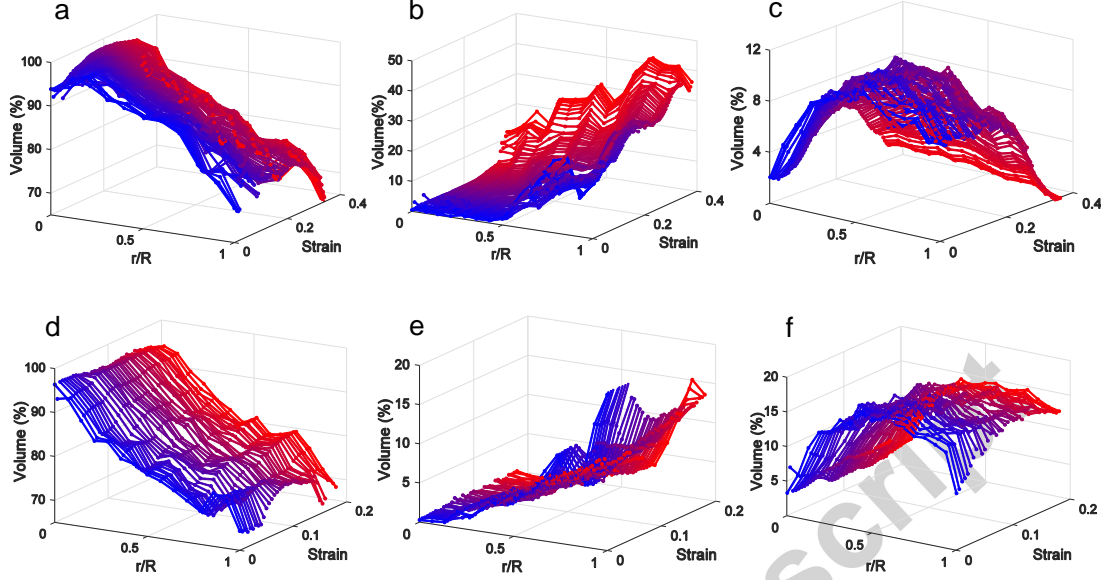


Figure 9 | In-Situ phase-volume evolution as a function of radial position and tensile strain in the gradient sample pre-twisted at 233K. (a) to (c) Evolution of phase volume fraction in the sample under tension at 300K: (a) F.C.C. phase volume; (b) B.C.C. phase volume; and (c) H.C.P. phase volume. (d) to (f) Evolution of the phase-volume in the sample under tension at 233K: (a) F.C.C. volume; (b) B.C.C. volume; and (c) H.C.P. volume.

The load partition accompanied with phase transformation during deformation is of particular interest in the gradient samples. We quantify the lattice strain of different phases as a function of radial position at different macroscopic strains when the tests were carried out at room temperature. Fig. 10a shows that for F.C.C. phase along the (200) planes, the core of the sample has the highest stress at the beginning of tension. With the increasing strain, the F.C.C. phase carries nearly the same level of stress along the radial direction. However, the B.C.C. phase near the edge bears more stress at first. With further stretch, the B.C.C. phase has uniform stress along the radial direction; see Fig. 10b. The load-carrying mode in the H.C.P. phase is similar to that of the F.C.C. phase, as seen in Fig. 10c. The phase information at -40°C tension is presented in Figs. 10d to 10f: The stress in the F.C.C. phase decreases from the core to the edge of the sample (Fig. 10d), and the same trend is seen in the H.C.P.

phase (see Fig. 10f). The B.C.C. phase in the edge bears higher load than that in the core, as demonstrated by Fig. 10e.

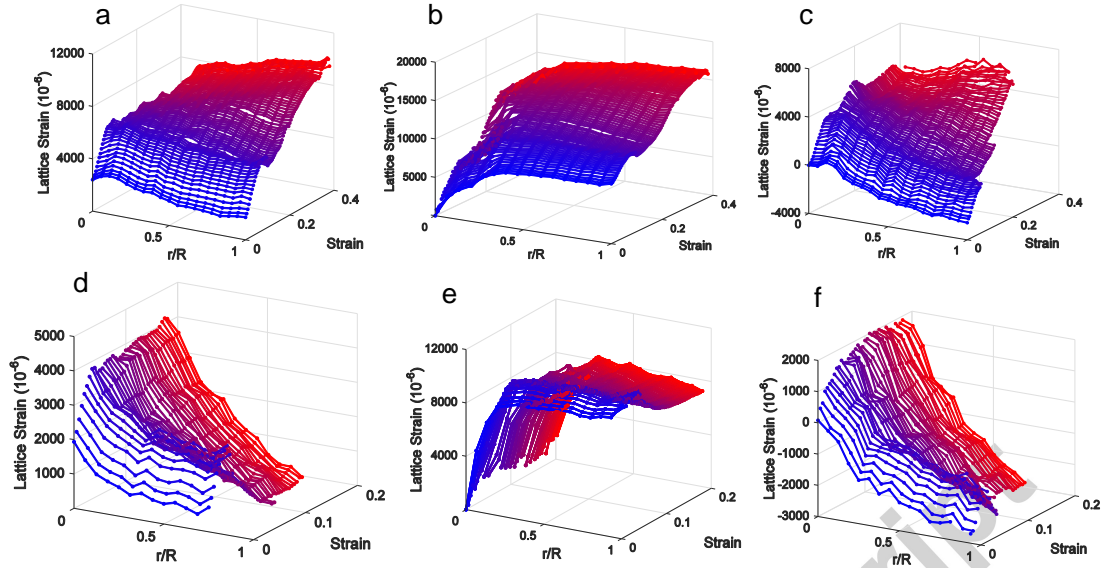


Figure 10 | In-Situ micro-strain evolution along the radial direction of the gradient sample by pre-twisting at 233K. (a) to (c) Evolution of the micro-strain in the sample under tension at 300K. The samples was subjected to a 360 degree pre-twist. We show in turn the micro-strain evolution as a function of the macroscopic tensile strain in different phases, (a) the F.C.C. phase along the (200) planes, (b) the B.C.C. phase along the (211) planes, and (c) the H.C.P. phase along the (10-10) planes. (d) to (f) Micro-strains of the samples under tension at 230K: (d) F.C.C. phase (200), (e) B.C.C. phase (211), and (f) H.C.P. phase (10-10).

4. Conclusion

In conclusion, we reported a novel gradient nanostructure design to enhance the cryogenic mechanical properties of traditional stainless steel by increasing its yield strength from 671MPa to 1745MPa at 77K while retaining a deformability of 23% plastic tensile strain. As being revealed by Fleck et al.³⁰ that the fatigue limit is proportional to the yield strength of a polycrystalline metal, we expect the fatigue performance at CT could be dramatically enhanced as well. Actually, according to these authors, the fatigue limit is proportional to the yield stress to the (1-m) power, where $m=0.3 - 0.5$. The significant improvement in strength is attributed to the following factors: (a) The phase gradient along the radial direction with a higher volume fraction of martensitic crystalline structures in the edge leads to optimal stress partition, with higher stress in the strong yet tough martensitic phase near the edge.

This helps to delay premature failure initiated from the surface. (b) Continual phase-transformation along the radial direction prevents the formation of large hydrostatic tension in the core and also supplies sufficient hardening required for deformability. (c) The high stress level triggers dislocation plasticity in martensitic crystalline structures, which is also beneficial to overall ductility and strength of the material. The introduced method could be broadly employed to enhance the cryogenic mechanical behaviours of steels and other alloys which could undergo phase transformation during plastic deformation at low temperature.

Acknowledgements

Y.Wei acknowledges the support from National Natural Science Foundation of China (NSFC) (11425211). Y. Wang acknowledges the financial support from National Natural Science Foundation of China (NSFC) (51231002). The use of the Advanced Photon Source was supported by the U.S. Department of Energy, Office of Science, Office of Basic Energy Sciences, under Contract No. DE-AC02-06CH11357. Fruitful discussion with Professor Ke Lu at IMR is sincerely appreciated.

References

1. Y. Kimura, T. Inoue, F. Yin, K. Tsuzaki. Inverse temperature dependence of toughness in an ultrafine grain structure steel. *Science* 320 (2008) 1057-1060.
2. National Research Council. Research Opportunities in Corrosion Science and Engineering. National Academies Press (2011).
3. M.F. Ashby. Materials Section in Mechanical Design 2nd edn. Butterworth-Heinemann (1999).
4. B. Gludovatz, A. Hohenwarter, D. Catoor, E.H. Chang, E.P. George, R.O. Ritchie. A fracture-resistant high-entropy alloy for cryogenic applications. *Science* 345 (2014) 1153-1158.
5. Q.J. Wang, Y.W. Chung. Ductile-to-Brittle Transition Temperature. Springer (2013).
6. M. Militzer. A Synchrotron Look at Steel. *Science* 298 (2002) 975-976.
7. S.H. Kim, H. Kim, N.J. Kim. Brittle intermetallic compound makes ultrastrong low-density steel with large ductility. *Nature* 518 (2015) 77-79.

8. K. Lu, et al. Making strong nanomaterials ductile with gradients. *Science* 345 (2014) 1454-1455.
9. K.M. Chang, C.G. Cha, T.F. Liu. Excellent combination of strength and ductility in an Fe-9Al-28Mn-1.8C alloy. *Scripta Materialia* 63 (2010) 162-165.
10. T.H. Fang, W.L. L, N.R. Tao, K. Lu. Revealing extraordinary intrinsic tensile plasticity in gradient nano-grained copper. *Science* 331 (2011) 1587-1590.
11. H. Kou, J. Lu, Y. Li. High-Strength and High-Ductility Nanostructured and Amorphous Metallic Materials. *Advanced Materials* 26 (2014) 5518-5524.
12. S. Suresh. Graded materials for resistance to contact deformation and damage. *Science* 292 (2001) 2447-2451.
13. H.J. Gao, B. Ji, I.L. Jager, E. Arzt, P. Fratzl. Materials become insensitive to flaws at nanoscale-Lessons from nature. *PNAS* 100 (2003) 5597-5600.
14. K. Lu, J. Lu. Surface nanocrystallization (SNC) of metallic materials-presentation of the concept behind a new approach. *J Mater Sci Technol* 15 (1999)193-197.
15. X.L. Wu, P. Jiang, L. Chen, F.P. Yuan, Y.T. Zhu. Extraordinary strain hardening by gradient structure. *PNAS* 111 (2014) 7197-7201.
16. Y.J. Wei, et al. Evading the strength-ductility trade-off dilemma in steel through gradient hierarchical nanotwins. *Nature Communications* 5 (2014) 3580.
17. I. Gutierrez-Urrutia, D. Raabe. Influence of Al content and precipitation state on the mechanical behavior of austenitic high-Mn low-density steels. *Scripta Materialia* 68 (2013) 343-347.
18. G. Bernd, H. Anton, K.V.S. Thurston, H. Bei, Z. Wu, E.P. George, R.O. Ritchie. Exceptional damage-tolerance of a medium-entropy alloy CrCoNi at cryogenic temperatures. *Nature Communications* 7 (2016) 10602.
19. S.Y. Liu, Y.J. Wei. The Gaussian distribution of lattice size and atomic level heterogeneity in high entropy alloys. *Extreme Mechanics Letters* 11 (2016) 84-88.
20. G.R. Garrett, M.D. Demetriou, M.E. Launey, W.L. Johnson. Origin of embrittlement in metallic glasses. *PNAS* 113 (37) (2016) 10257-10262.
21. Q. An, K. Samwer, M.D. Demetriou, M.C. Floyd, D.O. Duggins, W.L. Johnson, W.A. Goddard. How the toughness in metallic glasses depends on topological and chemical

heterogeneity. PNAS 113 (26) (2016) 7053–7058.

22. American Society for Testing and Materials. Standard Specification for Stainless Steel Bars and Shapes. A276-06.

23. W. Xu, N. Birbilis, G. Sha, Y. Wang, J.E. Daniels, Y. Xiao, M. Ferry. A high-specific-strength and corrosion-resistant magnesium alloy. Nature Materials 14 (2015) 1229.

24. M.L. Young, J.D. Almer, M.R. Daymond, D.R. Haefner, D.C. Dunand. Load partitioning between ferrite and cementite during elasto-plastic deformation of an ultrahigh-carbon steel. Acta Materialia 55 (2007) 1999-2011.

25. Z.W. Ma, J.B. Liu, G. Wang, H.T. Wang, Y.J. Wei, H.J. Gao. Strength gradient enhances fatigue resistance of steels. Scientific Reports 6 (2016) 22156.

26. J.T. Kim, et al. Deformation mechanisms to ameliorate the mechanical properties of novel TRIP/TWIP Co-Cr-Mo-(Cu) ultrafine eutectic alloys. Scientific Reports 7 (2017) 39959.

27. T.S. Byun, N. Hashimoto, K. Farrel. Temperature dependence of strain hardening and plastic instability behaviors in austenitic stainless steels. Acta Mater. 52 (2004) 3889-3899.

28. N. Li, Y.D. Wang, W.J. Liu, Z.N. An, J.P. Liu, R. Su, J. Lie, P.K. Liaw. In situ X-ray microdiffraction study of deformation-induced phase transformation in 304 austenitic stainless steel. Acta Materialia 64 (2014) 12-23.

29. X.L. Wu, M.X. Yang, F.P. Yuan, L. Chen, Y.T. Zhu Combining gradient structure and TRIP effect to produce austenite stainless steel with high strength and ductility. Acta Materialia 112 (2016) 337-346.

30. N.A. Fleck, K.J. Kang, M.F. Ashby. Overview No. 112: The cyclic properties of engineering materials. Acta Metall. Mater. 42 (1994) 365-381.